M2LW-21OR0402027

Light Water Reactor Sustainability Program

Electrochemical profiling of physical damage in nuclear core components

September 2021

U.S. Department of Energy
Office of Nuclear Energy

M2LW-21OR0402027

Electrochemical profiling of physical damage in nuclear core components

Xin Chen ([1]), Maxim Gussev ([2]), Gaurav Sant ([1])

[1] University of California, Los Angeles, CA, USA
[2] Oak Ridge National Laboratory, Oak Ridge, TN, USA

September 2021

Prepared for the
U.S. Department of Energy
Office of Nuclear Energy

EXECUTIVE SUMMARY

Overview: Plastic strain and irradiation damages render nuclear reactor components more susceptible to stress corrosion cracking (SCC) and irradiation-assisted SCC (IASCC). This work developed multiscale and multimodal approaches to concurrently profile physical damages and corrosion susceptibilities in nuclear alloys, rendering maps of SCC and IASCC susceptibilities at micro-to-macro scales. We have determined that, deformation and irradiation induced microstructures can demote the steel's surface impedance and stimulate corrosion activities. Indeed, we have obtained consistent corrosion rate and surface impedance in good agreement with allocations and magnitudes of strain concentrations and dpa doses. Significantly, the scanning probe analyses enable electrochemical pathways in tracing root-causes of irradiated, deformed, cracked, and failed nuclear components.

Implications: The methodology developed herein can be utilized to determine and predict SCC and IASCC susceptibilities while accommodating the complex geometry of nuclear alloy components. More importantly, as next generation reactors (e.g. the transformational Challenge Reactor, TCR) will likely employ additive manufacturing (i.e., selective laser melting, SLM) to adapt to an agile and continuously evolving design, the outcome of this work can also provide accurate and high-throughput approaches for screening the microstructural heterogeneities and degradation performances of the manufactured or in-service components.

ACKNOWLEDGEMENTS

The authors acknowledge financial support for this research from the U.S. Department of Energy's Light Water Reactor Sustainability (LWRS) Program through the Oak Ridge National Laboratory operated by UT-Battelle LLC (Contract #: 4000154999). The contents of this paper reflect the views and opinions of the authors who are responsible for the accuracy of data presented. This research was carried out in the Laboratory for the Chemistry of Construction Materials (LC^2) and the California Nanosystems Institute at UCLA. As such, the authors gratefully acknowledge the support that has made these facilities and their operations possible.

CONTENTS

FIGURE CAPTIONS

TABLE CAPTION

Electrochemical profiling of physical damage in nuclear core components

1. Introduction

Alloy degradation has been accompanied by our metal-based civilization for thousands of years; its costs are still beyond estimation as of today. After entering the nuclear-era, metals have been acclimatized to more acute environments in nuclear power plants (NPPs) and nuclear waste disposal facilities[1], wherein alloys can be damaged physically (e.g., via deformation and irradiation)[2,3], electrochemically (e.g., via corrosion)[4], or via synergetic pathways (e.g., stress corrosion cracking [SCC], irradiation-assisted SCC [IASCC], etc.)[5,6]. Damage quantification is critical in understanding alloy degradation, preventing catastrophic failure, and screening failure-resistant materials for nuclear applications. However, the task is challenging due to the divergence of damage types and the damage allocation at micro-to-macro scales[7]. For instance, the prevailing analytical approaches can only partially reveal either an alloys' microstructural or corrosion behaviors—at dedicated scales and surface conditions. For example, electron diffraction methods yield localized microstructural damages at the sub-mm scales[8–10]; whereas conventional non-destructive analyses (e.g., ultrasonic, eddy current methods) only acquiesce bulk physical damage while overlooking localized features[11,12]. Likewise, corrosion susceptibility assessments for nuclear alloys remain underdeveloped, as of now, the reported corrosion behaviors were mostly elucidated by localized oxides characteristics[13,14] or the bulk corrosion potentials[15,16].

Corrosion, mechanical, and irradiation damages jointly render nuclear alloys susceptible to SCC and IASCC. Therefore, forecasting SCC and IASCC requires integrated assessments of corrosion and physical damages, preferably, simultaneously. In this study, we have demonstrated the surface electrochemical reactivities are in synergy to strain-induced microstructural heterogeneities in austenitic stainless steels, even though the heterogeneities (e.g., martensite, point defects, dislocations which are induced through diffusion-less phase transformations) are identical in composition with the pristine matrix (austenite)[4]. Further, irradiation damage resembles (to an extent) deformation damages, as irradiation also stimulates point defects and dislocation loops[17]. Similarly, irradiation-induced microstructural heterogeneities have been observed to alter surface reactivities when positioned in aqueous solutions (e.g., reactor coolant, permeated ground water, etc.)[18]. Hence, by using the interconnections between corrosion behaviors and strain- and irradiation- induced microstructures, the allocation and extends of physical damages can be potentially determined via electrochemical analyses.

It therefore requires spatially resolved electrochemical characterization methods to unravel the localized corrosion susceptibility. To this end, the scanning Kelvin probe force microscopy (SKPFM) and scanning electrochemical microscopy (SECM) were employed herein to determine steel's surface reactivity in both the ambient and aqueous environments. Additionally, we use the scanning electrochemical cell microscopy

(SECCM) approach to achieve multiscale, multimodal electrochemical analyses on nuclear alloys. The technique employs a micropipette to conduct spatially resolved electrochemical characterizations[19,20]. By performing localized amperometric, potentiometric, and impedance analyses, we seek to highlight surface anomalies in corrosion behaviors, and to quantify the SCC and IASCC susceptibilities in stainless steels stimulated by strain- and irradiation- induced lattice transformations.

2. Experimental

Sample preparation: A hot rolled 304L stainless steel (ArcelorMittal) with the nominal composition listed in **Table 1** was sectioned into miniature tensile specimens shown in **Figure 1a**. The specimens were elongated to 5%, 10%, 22%, and 30% strain under uniaxial tension at a strain rate of 5×10^{-4}/s. To make electrodes, the gauge parts of each sample were sectioned using a low-speed diamond wafering saw and attached to a lead wire. The assemblies were then embedded in epoxy resin, and the exposed surfaces were successively polished (N.B., with using the 50 nm colloidal silica as the final step) until the surface featured a mean-roughness $S_a < 10$ nm.

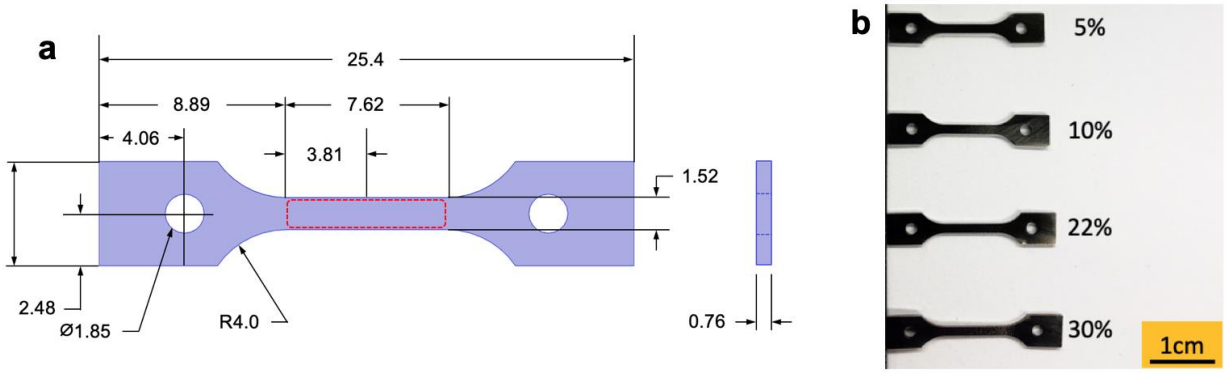

Figure 1. (a) A schematic shows the geometry of the miniature tensile sample used in this work, the dimensions are in mm. (b) The optical photo of the progressively deformed samples.

Table 1. The chemical composition of the 304L stainless steel used (mass %).

Fe	Cr	Ni	Mo	Mn	N	C	Si
bal.	18.29	8.02	0.07	1.28	0.05	0.02	0.45

Irradiation: A 304L steel specimen was annealed at 1050 °C for 3 h to produce solution-treated monophasic austenitic microstructure, with grain size on the order of tens of micrometers. The specimen was subsequently irradiated at 300 °C by using a 2 MeV proton ($[H^+]$) beam until a target fluence of 1.84×10^{19} ions/cm^2 was attained. Such irradiation resulted in a 20 μm irradiated layer with the peak dose of 21 dpa attained at the 18 μm depth. A flat-region irradiation damage of 1.11 dpa was calculated based on the full-cascade SRIM simulations.

Microstructure characterization: The crystallographic orientations of the grains were determined using a Scanning Electron Microscopy (SEM, Tescan Mira3) equipped with an EBSD detector (Oxford Ultim Max). The acceleration voltage and step size used were 20 kV and 500 nm, respectively. The EBSD data were subsequently analyzed using the OIM Analysis® software. A magnetic phase detector (Fisher technology FMP30) was used to detect the ferrite and martensite contents of the steel specimens prior and post to deformation.

Surface reactivity analysis: The surface reactivity of the deformed and [H^+]-irradiated 304L steels were evaluated using a scanning electrochemical microscope (SECM, HEKA ElProScan). The SECM is equipped with a 10 µm Pt ultramicroelectrode (UME) with the RG ratio, i.e., the ratio of the glass-sheath-radius to the Pt-UME-radius, close to 3. The SECM tests were performed with samples immersed in 0.1 and 0.2 M LiCl solutions (pH 5.8) with 2 mM hexaammineruthenium chloride ($Ru(NH_3)_6Cl_3$) as the redox mediator. (N.B., the Li-BBS was not used in SECM measurements to avoid potential complexations between the borate ions and the redox mediator.) A -0.35 $V_{Ag/AgCl}$ potential was applied to the UME to promote the diffusion-limiting current of the redox mediator reduction. The surface reactivity was measured using the SECM operated under approaching and constant-distance modes. The former was performed by holding slowly approaching the Pt UME (1 µm/s) to the sample surface while acquiring the current evolution; the latter was performed by tapping the UME to the surface and then lift to a constant distance (~5 µm) and scanning the surface point-to-point.

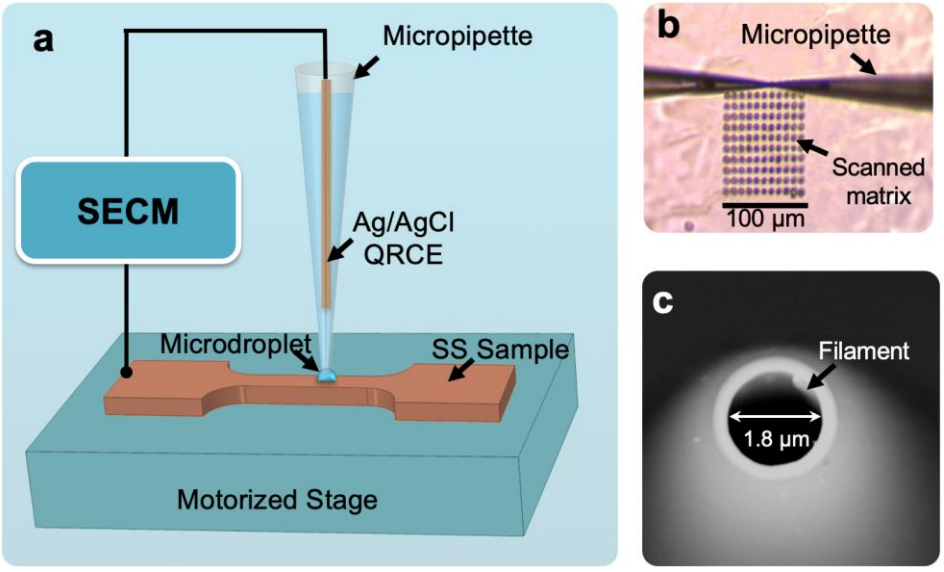

Figure 2. (a) A schematic of the SECCM setup developed using the scanning electrochemical microscope (SECM). (b) An optical photo showing a scan in progress. (c) SEM image of the micropipette used in this study.

As for the scanning electrochemical cell microscopic (SECCM) measurements, the SECM was equipped with micropipettes with a 1.8 ± 0.3 µm opening (see **Figure 2c**).

The SECCM tests were performed with the micropipettes filled with 0.2 M LiCl or 0.2 M LiCl + 5% HNO_3 solutions. N.B., the LiCl as a potential coolant contaminant, was used herein to promote measurable corrosion signals; and the 0.2 M LiCl + 5% HNO_3 are used to reveal corrosion resistance of only the barrier oxide film with surface hydroxides readily dissolved. During scanning, the steel samples were connected as the working electrode and an AgCl-coated silver wire was inserted in the micropipette to serve as the quasi-reference-counter-electrode (QRCE). When the micropipette approaches the steel surface, a 30s open circuit hold was performed allowing microdroplets to stabilize. The open circuit potentials (OCP) were measured at the end of the hold. Thereafter, potentiodynamic (PD) polarization was performed at -0.25 V_{OCP} to 0.4 V_{OCP} with a 20 mV/s scanning rate. Electrochemical impedance spectroscopy (EIS) was conducted at OCP with ± 10 mV stimulus potential over the frequency range of 10 kHz to 1 Hz. A programmable 3D motor with nanometer precision controlled the positioning of the micropipette to scan a grid-matrix that is superimposed on EBSD- and optical microscope mapped areas. This produced hundreds of location-specific corrosion datasets within one scan (see **Figure 2b**), and allowed correlation of measured properties (e.g., corrosion rate, corrosion potential, and passive film thickness, etc.).

Surface topography and potential analysis: The topography of polished samples was measured using atomic force spectroscopy (AFM, Bruker Dimension Icon) operated under the tapping mode. The amplitude-modulated Kelvin probe force spectroscopy (AM-KPFM) was performed using an antimony-doped silicon oxide tip (Bruker PFQNE-AL) with a calibrated work function of 4.09 eV[21].

All experiments were performed at the room temperature (23 ± 2°C). All chemicals used in this study are ACS reagent grade. Solutions were prepared with deionized (DI) water (>18 MΩ-cm^2).

3. Results and discussion

3.1 Post-yielding microstructural analysis

The steel's microstructure evolution is the prerequisite governing the development of corrosion activities, and it was therefore characterized as the first step. As functions of the bulk strain, lattice defects, encompassing dislocations and strain-induced phases were revealed by the EBSD analyses as shown in **Figure 3**.

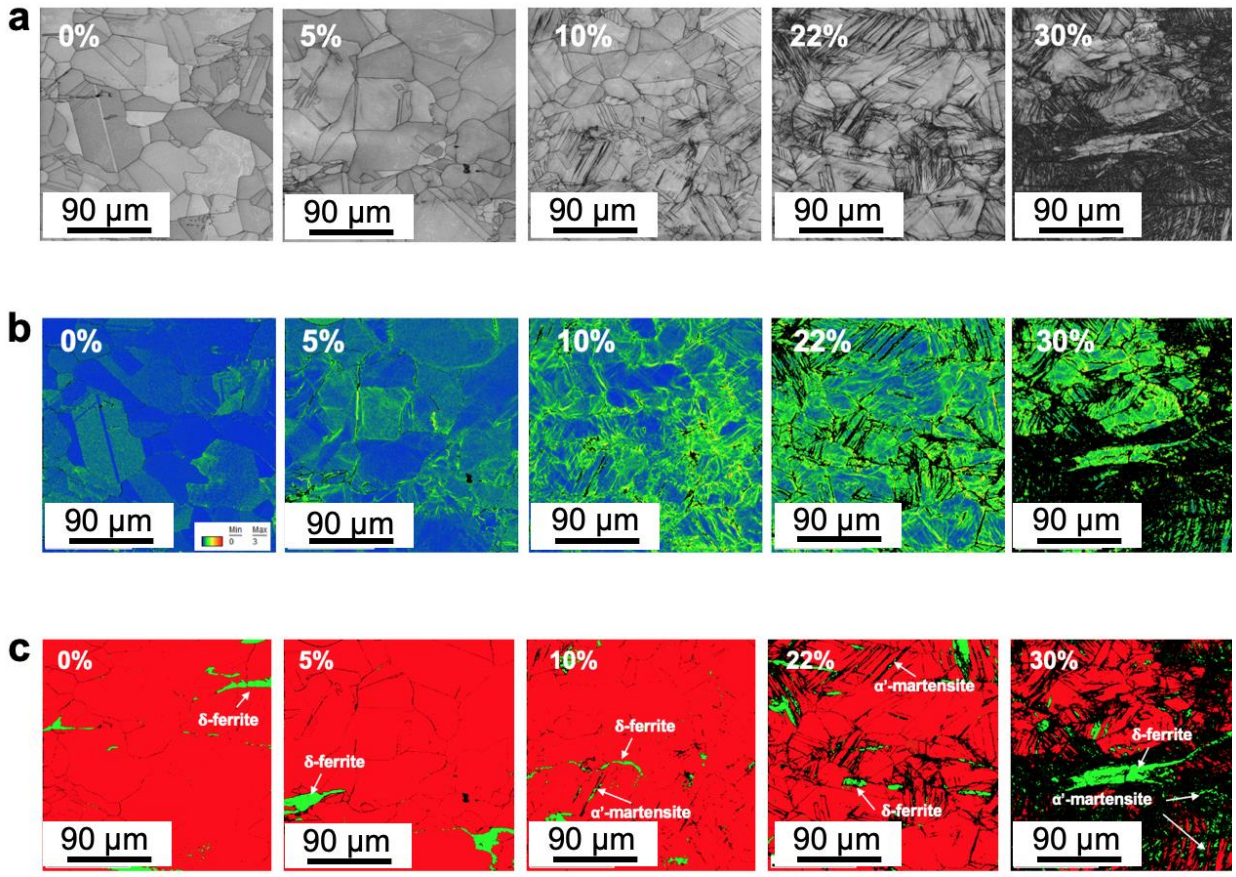

Figure 3. The strain-induced microstructure evolution was analyzed by EBSD. **(a)** Image quality (IQ) maps show the buildup of microstructural defects resulted from the bulk deformation. The localized strain is revealed by the kernel average misorientation (KAM) maps shown in **(b)**, and the development of strain-induced α'-martensite is shown in **(c)**.

As the most common strain-induced defect, dislocations create elastic fields in the surrounding lattice and retain mechanical energy (i.e., the stored energy), thus elevating the chemical energy of steel atoms[22]. Therefore, the dislocation density is closely related to the corrosion reactivity. Specifically, the accumulation of geometrically necessary dislocations (GND) drives grain rotation during tensile testing, and the GND density can be revealed by the kernel average misorientation (KAM) analysis[10]: $\rho_{GND} = \frac{2\vartheta}{b\mu}$ [**Eq. 1**], where ϑ is the KAM angle, b is the magnitude of burger's vector, and μ is the EBSD step size (500 nm). As seen from **Figure 3b**, the distribution of dislocations is not uniform at the microscale. The KAM maps highlight the localized variation in GND densities, for instance, regions adjacent to grain and phase boundaries are often of high KAM angles, indicating higher dislocation concentration, and, therefore, stored energy in these regions. Stemmed from the localized accumulation of dislocations, the averaged GND densities also increase proportionally as a function of the bulk strain (see **Figure 4a**). Note that, the GND density was calculated using the area-averaged KAM values.

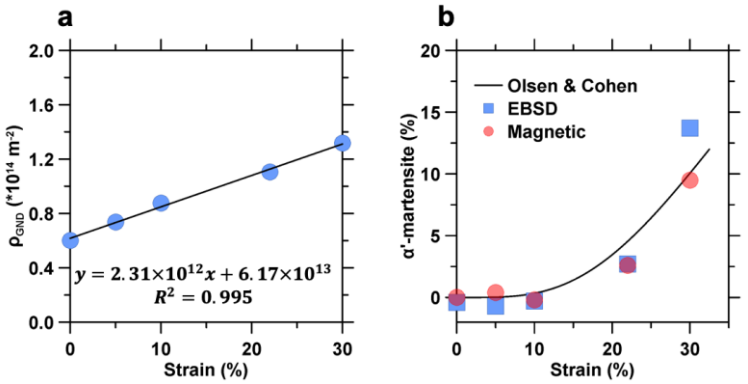

Figure 4. Quantification of post-yielding microstructures as functions of the bulk strain: **(a)** the densities of geometrically necessary dislocations and **(b)** the α'-martensite contents as measured using the EBSD and a magnetic phase detector. The δ-ferrite contents were measured prior to deformation, and were subtracted in both measurements. The solid line represents the theoretical martensite content calculated based on the Olson-Cohen model[23].

On the other hand, dislocation development can only result in a limiting localized misorientation angle of < 2°, further microstructural heterogeneity is attributed to the strain-induced phase transformations. Among the strain-induced phases, the large α'-martensite domains has a body-centered-cubic (bcc) structure and a lath-like morphology, thereby can be revealed by the phase map shown in **Figure 3c.** Based on the volumetric analyses (as shown in **Figure 4b)**, detectable amounts of strain-induced α'-martensite emerged in the 10% deformed sample and grew in volume as the strain increases. In addition, a large fraction of small martensite domains and deformation bands render poor electron diffraction patterns, they are denoted as dark areas in the image quality (IQ) as well as the other EBSD maps. By comparing the KAM and phase distribution images, one can notice that the deformation bands and martensites preferentially develops at dislocation concentrated areas, suggesting the dislocation accumulation stimulates the strain-induced phase transformations. This assertion can also be confirmed by the observation that, strain-induced phases are generally allocated adjacent to δ-ferrite inclusions, which can impede dislocation motion and cause dislocation accumulation[24].

Unlike dislocation formation processes, strain-induced phase transformations are usually exothermic[25], implying the resulted phases do not directly contribute to the stored energy[26]. However, due to the microstructurally defective nature of deformation bands and the α'-martensite, their roles in inducting localized corrosion were subsequently assessed.

3.2 Determining strain-activated bulk corrosion susceptibility.

In order to correlate the steel's post-yielding microstructure with corrosion reactivity, the progressively deformed samples were characterized via electrochemical means. A detreated borate buffer solution was used to represent a chlorine-contaminated reactor coolant composition. In this solution, equilibrium potentials (i.e., corrosion potentials) were measured following a one-hour immersion. As a result, evident reduction in corrosion potentials were observed as the bulk deformation increases (**Figure 5a**): for instance, the corrosion potential of the 30 % deformed 304L is about 60 mV lower than the undeformed control. This indicates that, strain-induced microstructures clearly lead to bulk corrosion instability of the 304L. More importantly, the corrosion potentials are decisive of the galvanic series of alloys[27], the greatly deformed samples are therefore less noble than samples with smaller amounts of strain.

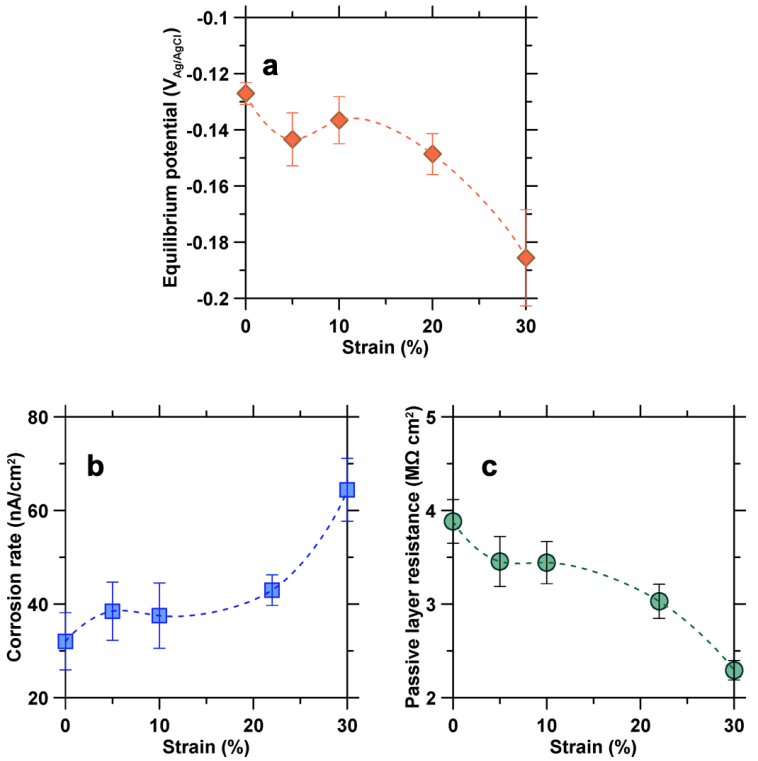

Figure 5. Quantification of strain-induced bulk corrosion behaviors of the 304L stainless steel: **(a)** reduction in equilibrium potential **(b)** enhanced corrosion rates and **(c)** deteriorated passive layer resistances. The experiments are conducted in the deaerated borate buffer solution with lithium chloride, 0.0375 M $Li_2B_4O_7$ + 0.15 M H_3BO_3 + 0.1 M LiCl (pH 8.4).

Such insights are also supported by the anodic behaviors of deformed 304L in the same solution. An anodic potential of 0.1 $V_{Ag/AgCl}$ was applied to simulate an

oxidizing reactor environment resulting from reactor coolant radiolysis[7,28,29]. When polarized, the 304L steel passives and its corrosion current attains a steady-state rate after a two-hour potentiostatic hold. The steady-state corrosion rate (as shown in **Figure 5b and 5c**,) doubled from 32 nA/cm^2 to 64 nA/cm^2 as the deformation increased from 0 to 30 %, whereas the passive layer resistance reduced from 3.9 MΩ cm^2 to 2.3 MΩ cm^2, also by a factor of ~2. As evidenced, the formation of less resistant passive layers can also be attributed to the post-yielding microstructures. This is significant since, in reactor environments, the passive layer impedes the steel's redox interactions with the strong oxidant produced by coolant radiolysis (e.g. hydroxyl radicals and H_2O_2)[30], and defective passive layers enhance steel's in-reactor reactivity.

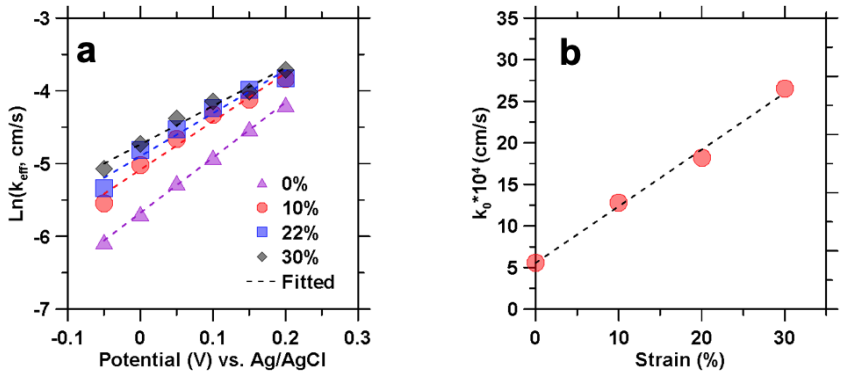

Figure 6. The change in steel's surface reactivity is also sensitive to the amount of strain. **(a)** Tafel plots show a clear dependence of k_{eff} with the amount of strain. **(b)** Consistently, the calculated k^o is linearly proportional to the strain. These SECM tests were conducted using the approaching mode in a solution of 0.1 M LiCl+ 2 mM $Ru(NH_3)_6Cl_3$ (pH 5.8).

As such, SECM was employed to characterize the surface reactivity availed by post-yielding microstructures. By adding a trace-amount of redox mediator (2mM $Ru(NH_3)_6Cl_3$) in solution, the SECM measures the reduction current of the following reaction:

$$Ru(NH_3)_6{}^{3+} + e^- \rightarrow Ru(NH_3)_6{}^{2+} \quad (1)$$

A diffusion-limiting reduction current, I_0, was attained when the SECM probe (i.e., the Pt ultramicroelectrode, UME) was far away from the steel surface. By approaching the Pt UME towards the steel surface, the UME-reduced $Ru(NH_3)_6^{2+}$ was oxidized by the steel surface to form $Ru(NH_3)_6^{3+}$ (through the reverse process of **Reaction 1**). Then the SECM probe acquired the feedback from surface-generated $Ru(NH_3)_6^{3+}$, and measured an integrated current I_{UME}. The reactivity of steel's passive film is characterized by the generation rate constant of $Ru(NH_3)_6^{3+}$, k_{eff} (in cm/s), which can be quantified by analyzing the approach curve of the normalized UME currents (I_{UME} / I_0).)

As shown in the Tafel plots (**Figure 6a**), at a fixed amount of strain, the k_{eff} dependence with the applied potentials are well-governed by the Butler-Volmer

relationship[31]: $k_{eff} = k^o \exp[\frac{\alpha n F}{RT}(E - E^{0'})]$ [**Eq. 2**], where k^o is the standard rate constant, α is the charge transfer coefficient, n is the number of electrons, F is the Faraday constant, R is the gas constant, T is the temperature, E is the applied potential, and $E^{0'}$ is the standard potential of the $Ru(NH_3)_6^{3+/2+}$ redox couple. As depicted in **Figure 6b**, the regressed k^o coincide with k_{eff}, both of which were elevated by the post-yielding strain, indicating that post-yielding microstructures renders more reactive surface. In fact, the observations are consistent with the measured surface reactivity of the 304L when subjected to only elastic stresses[32,33]. And similar surface reactivity enhancement has also been observed for the Ni-based austenitic alloys under both compressive and tensile stresses[34]. Taken together, the post-yielding microstructures activate the surface reactivity in a similar way as the elastic stresses, i.e., by inducing defects in passive films and to synergize charge transfer reactions at the film/solution interface. Consequently, the surface reactivity of the 304L steel is governed by the amount of deformation, yielding a linear dependence of k^o on the strain.

3.3 Assessing the impact of micro-galvanic corrosion

As the localization of post-yielding microstructures is evident based on EBSD analyses (**Figure 3**), the steel surface may not exhibit uniform corrosion activities. For instance, due to the increasing strain resulted in reduction of bulk corrosion potentials (**Figure 5a**), the localized potential gradient – a key element to induct micro-galvanic corrosion – is likely to rise owing to the strain localization. Thus, the surface potential distribution in a 10% deformed 304L was assessed using SKPFM. The results (see **Figure 7a-d**) reveal that, the strain-induced α'-martensite, and shear bands exhibit surface potentials (i.e., Volta potentials) about 60 mV lower as compared to the austenitic matrices. Such potential difference is consistent with the corrosion potential reduction measured in solution (**Figure 5a**), implying the reduction in bulk corrosion potential stemmed from the development of α'-martensite and deformation bands. (N.B., based on our results, the SKPFM is not able to detect any surface potential variation related to dislocation concentrations.) The lower Volta potential corresponds to the lower energy cost to extract electrons via charge transfer reactions[35,36], and an excellent correlation has been established between the Volta potential and in-solution corrosion potentials[37]. Therefore, the α'-martensite and deformation bands are electrochemically less noble than the austenitic matrix. The micro-galvanic corrosion is expected to take place, wherein the strain-induced phases preferentially corrodes as the anode, whereas the austenite is catholically protected.

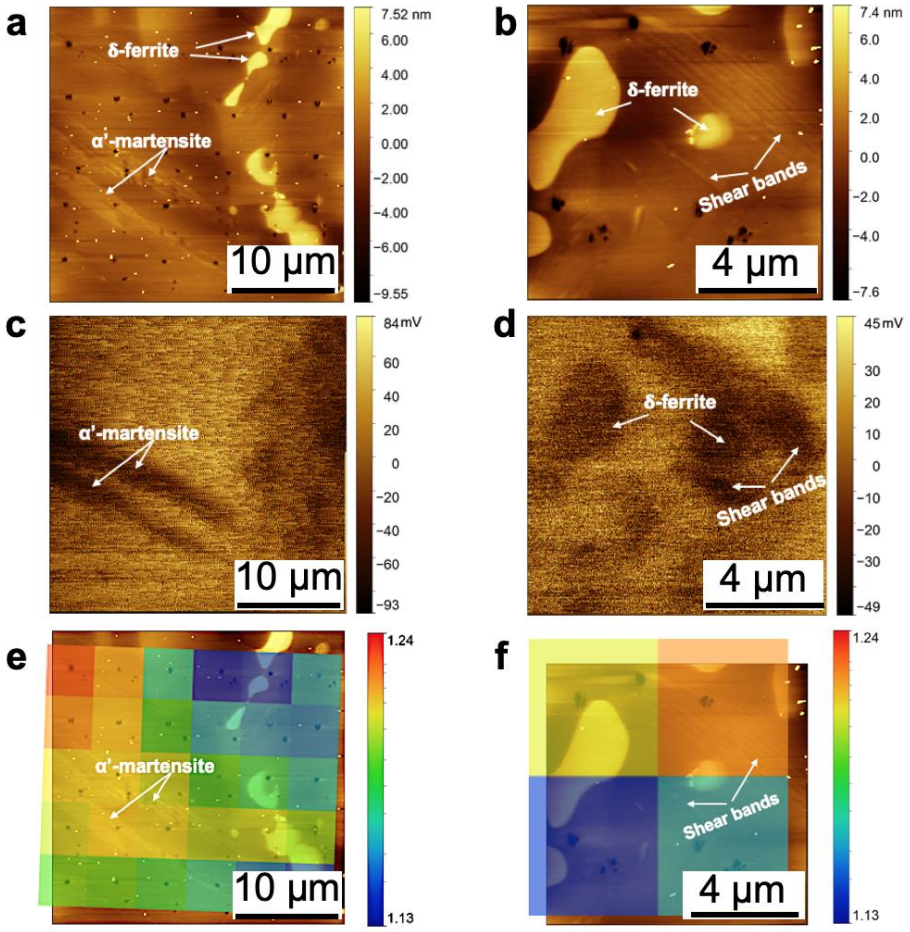

Figure 7. Apart from the lattice defects, the strain-induced phases also play critical roles in promoting localized corrosion. **(a)** and **(b)** are AFM-topography maps shown the strain-induced α'-martensite and deformation bands, which are also of lower surface potentials (i.e., Volta potentials) as compared to the austenite as shown in the SKPFM maps (**(c)** and **(d)**). This localized potential gradient give rise to micro-galvanic corrosion, as shown in **(e)** and **(f)**, the surface reactivities of strain-induced phases are evidently higher. The SECM tests were conducted using the constant-distance mode in a solution of 0.2 M LiCl+ 2 mM $Ru(NH_3)_6Cl_3$ (pH 5.8).

To profile the micro-galvanic corrosion at the steel surface, constant-distance SECM analyses were performed: the Pt UME were halted at 3 μm above the SKPFM-scanned area and measured the redox mediator's reaction current. As depicted in **Figure 7e and 7f**, the higher current is consistently observed at the lower surface potential areas, indicating the strain-induced α'-martensite and shear bands also have higher surface reactivity as compared to the less reactive austenite. These multimodal analyses demonstrated the strain-induced phases are subjected to accelerated corrosion owing to the micro-galvanic coupling.

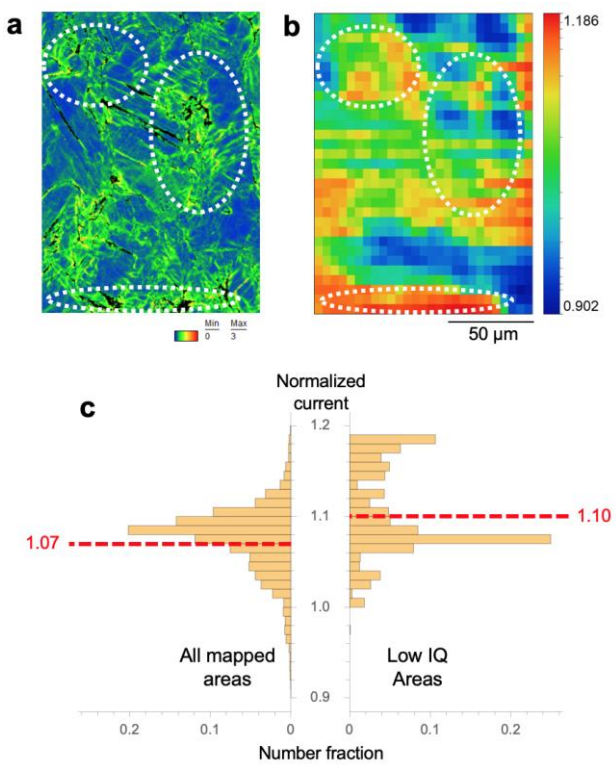

Figure 8. The strain localization can lead to localized corrosion. For example, a good correlation was identified between the **(a)** KAM map, and **(b)** SECM surface reactivity map of the 10% deformed tensile specimen. **(c)** shows the probability distribution of the normalized current from (left) all mapped areas, and (right) the strain-induced phases represented by the low image quality areas. The SECM tests were conducted using the constant-distance mode in a solution of 0.2 M LiCl+ 2 mM $Ru(NH_3)_6Cl_3$ (pH 5.8).

The EBSD results showed the localization of post-yielding microstructures, the micro-galvanic corrosion activities are likely to follow. As such, the EBSD-KAM and SECM-surface reactivity were mapped and compared from the same area of the steel surface (**Figure 8**). As indicated by the circled regions in **Figure 8a and 8b**, higher surface reactivities are generally associated with higher strain concentrations. In particular, **Figure 8c** shows that the strain-induced phases (represented by the low IQ areas, i.e., the dark regions shown in **Figure 8a**) were disposed to exhibit upper-bound currents, and the average is also higher vis-à-vis all measured areas. Furthermore, the circled regions are also indicative of that, the areas of higher reactivity are generally associated with larger KAM angles. As aforementioned, greater KAM angles denote

higher dislocation concentrations, consequently, higher stored energy is stored in these areas that activates surface reactions and steel corrosion.

On the other hand, because the SECM readily integrated responses from crystallographic features, e.g., grain boundaries and grain orientations[38], the convoluted surface reactivity distribution is not entirely in congruent with the strain localization when measured at grain-level scales. For instance, mismatches between the surface reactivity and KAM maps can be observed in **Figure 8**. By excluding such crystallographic influences, the impact of micro-galvanic corrosion was evaluated at a macro-scale that encompasses hundreds of diversely oriented grains.

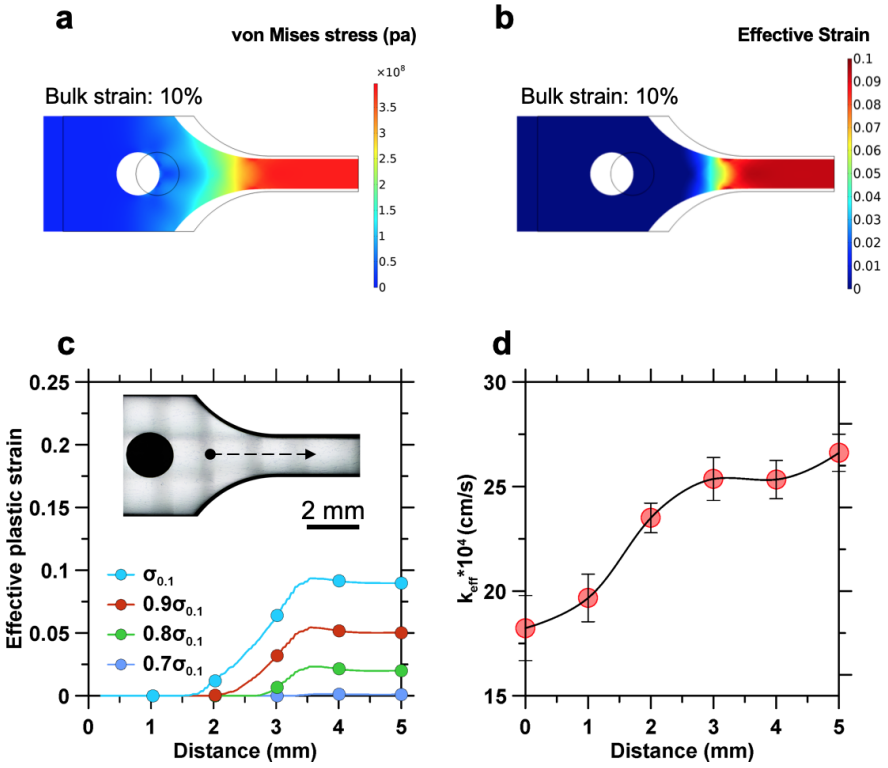

Figure 9. The plastic strain activated bulk corrosion sensitivity can be assessed by using the SECM. **(a)** The COMSOL® simulated von Mises stress and **(b)** the effective strain distributions of the tensile specimen deformed to a 10% bulk strain. **(c)** Simulated strain distributions along the arrow shown in the inset ($\sigma_{0.1}$ represents the stress required to attain the 10% bulk strain), and **(d)** regressed surface reactivity from the same locations shown a consistent distribution with the plastic strain. The SECM tests were conducted using approaching mode in a solution of 0.2 M LiCl+ 2 mM $Ru(NH_3)_6Cl_3$ (pH 5.8).

The macro-scale strain is expected to vary in the tensile specimens employed by this work (**Figure 1a**). A COMSOL® simulation was performed to determine the stress-strain distribution in the bulk. The simulation utilized a nonlinear elastoplastic model, wherein the post-yielding stress-strain relation is defined by the Ludwik relationship[39]: $\sigma_{ys} = \sigma_{ys0} + k(\varepsilon_{pe})^n$ [**Eq. 3**], where σ_{ys} is the stress beyond the yielding point, σ_{ys0} is the

yield stress (215 MPa), ε_{pe} is the effective plastic strain, and k (1033 Mpa) and n (0.768) are coefficients fitted from the experimental true-stress-strain curve. Based on the simulated results (**Figure 9a and 9b**), the post-yielding strain distributed uniformly at the gauge part but lessened at regions closed to the sample's head. The line profiles shown in **Figure 9c** depict the progressively increasing and then plateaued effective strain under successively increased stresses.

Due to the effective strain accumulated at the gauge part, it is expected to have concentrated strain-induced microstructures and pronounced corrosion micro-galvanic activities. In fact, as shown in **Figure 9c and 9d**, greater k_{eff} values were exhibited by the gauge part, whereas the tensile head is relatively inert. The distribution of surface reactivity is in congruent with that of the plastic strain. Interestingly, the micro-galvanic coupling resulted in a partitioned macro-corrosion reactivity. This implies that, localized corrosion is favored to initiate in the component with higher amount of deformation, wherein acute micro-galvanic corrosion can lead to the formation of micro- pits and crevices, which can further develop into SCC cracks. As for a propagating SCC crack, the micro-galvanic corrosion also explains why the plastic zone oxides at much faster rates[40,41]. Through surface reactivity analyses, the SECM provide feasible means to detect or predict the SCC susceptibilities at the micro- and bulk- scales.

3.4 Scanning probe polarization and AC-impedance analysis

We have demonstrated that, localization of post-yielding microstructures avails the SCC events in reactor components. Indeed, for many alloy components, SCC readily occurs in strain concentrated areas. Therefore, we have applied potentiodynamic (PD) polarizations to scan over an EBSD-mapped area on a 30% deformed 304L (see **Figure 2**). The characterized area is located adjacent to a retained δ-ferrite inclusion, which impedes dislocation motion and causes strain localziation[24]. Indeed, the EBSD reveals the strain distribution in this area are not uniform, most of the strain-induced phases, i.e., dislocation, deformation bands, and martensites are accumulated surrounding the δ-ferrite and denoted as low image quality (IQ) areas. Consistently, Tafel-fitting of the PD curves yield conventionally recognized corrosion currents (Icorr), the map of which also highlighted the same area with greater strain concentration (45-60 μA/cm^2, as compared to a 30-40 μA/cm^2 for less deformed regions see **Figure 10d**). Note that the PD curves were acquired within the microdroplets covered areas (~ 7 μm^2), as a result, the Icorr map represents localized corrosion rate of strain-induced phases *per se*. Once these phases are galvanically coupled with less deformed areas, the corrosion rate is expected to be higher[4]. The combined strain-hardening and localized corrosion will lead to greater possibility of crack initiation, in line with our SECCM-Icorr map, the SCC initiation are often observed close to the δ-ferrite[42].

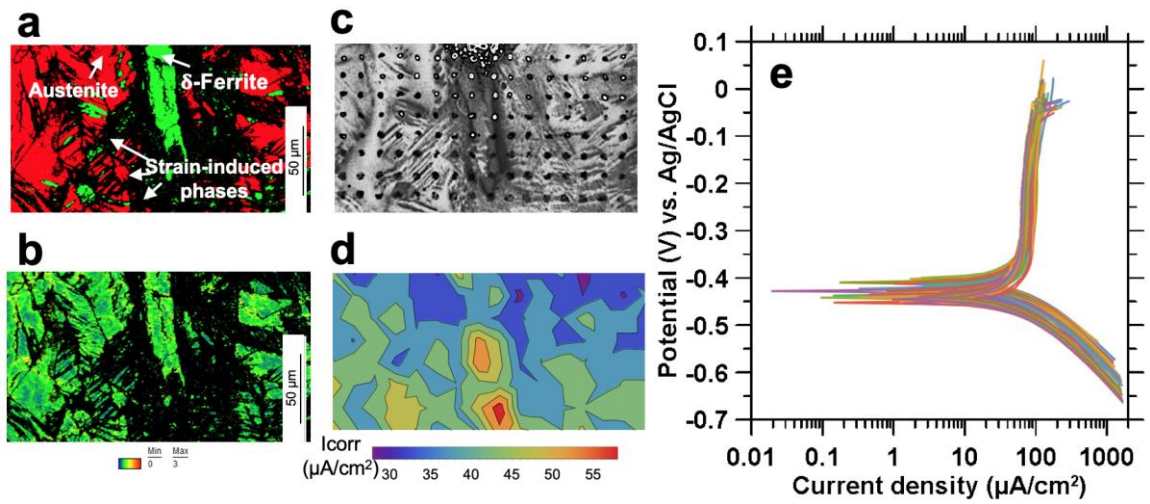

Figure 10. Scanning probe polarization analysis: (a) and (b) are, respectively, EBSD-phase and kernel average misorientation (KAM) analyses showing the strain localization in a 30% deformed 304L. (c) Polarized light microscope images show the 8 × 16 microdroplet matrix where the polarization tests were performed. The microdroplets are ~ 3 μm in diameter. (d) Contour plot of the Icorr values regressed via Tafel fitting the polarization curves shown in (e). A 20 mM LiCl solution was used in the PD tests.

While the scanning probe polarization analysis maps SCC susceptibility, it dynamically polarizes the substrate to non-equilibrium potentials (i.e., other than OCP) and can stimulate pitting corrosion during anodic sweeps. Further, the DC-based techniques become less sensitive as the surface oxide layers grow thicker and impedes charge-transfer between the substrate and solutions. Confined by microdroplets, picoampere (pA) current sensitivity is needed to resolve polarization curves of stainless steels passivated at room temperature, whereas oxide scales formed at higher (p,T) conditions can only permit femtoampere charge-transfer currents. Therefore, we have combined the scanning probe technique with the electrochemical impedance spectroscopy (EIS) so as to resolve surface reactivities in the form AC-impedances.

As the first step of scanning AC-impedance experiments, frequency-sweep EIS measurements were conducted on a 3×3 matrix over two grains characterized by distinct features (**Figure 11a**). The upper left four points were located on a severely deformed grain filled with strain-induced martensites and deformation bands; whereas the lower right four points were located on an austenitic grain with less strain concentration; and the center point is in super position with the grain boundary. A micropipette with a 1.8 μm tip opening were filled with a 0.2 M LiCl + 5% HNO_3 solution, after a 30 s OCP hold, the induced microdroplets were stabilized at 7-10 μm in diameter (**Figure 11a**). EIS was performed at the OCP with only small potential stimulus (± 10 mV) over a range of frequencies (10 kHz to 1 Hz). The two grains are characterized by distinguished impedance spectra that were plotted against positions of microdroplets (**Figure 11b**). Aimed at quantifying corrosion resistances, EIS spectra were fitted by a simplified Randles circuit (**Figure 11c**), where R_S is the solution resistance, R_{CT} and

CPE_{OX} respectively represent the charge transfer (corrosion) resistance and capacitive response of the passive film. The regressed corrosion resistance (R_{CT}) indicates the less deformed grain is ~1.7 fold more resistant to charge transfer (3.4 ± 0.5 kΩ-cm^2) as compared to the martensitic grain (2.0 ± 0.5 kΩ-cm^2). In nuclear environments where strong oxidants are produced by radiolysis (e.g. hydroxyl radicals and H_2O_2)[30], the passive layer is the main barrier impeding the steel's fast oxidation. Thus, defective passive layer promotes greater corrosion rates, that is in line with the observed fast-and-localized oxidation of strain-induced defects (deformation bands, α'-martensite, and dislocation networked areas) in reactor environments[43,44]. And therefore, the scanning EIS spectra offers reasonable prediction on grain-dependent SCC resistances.

Note that, the centered droplet covering the grain boundary show an intermedium resistance (2.5 kΩ-cm^2), resulting from the weighing average of both grains. This suggests the grain boundary, without sensitization or irradiation-induced segmentation, is not evidently susceptible to intergranular corrosion.

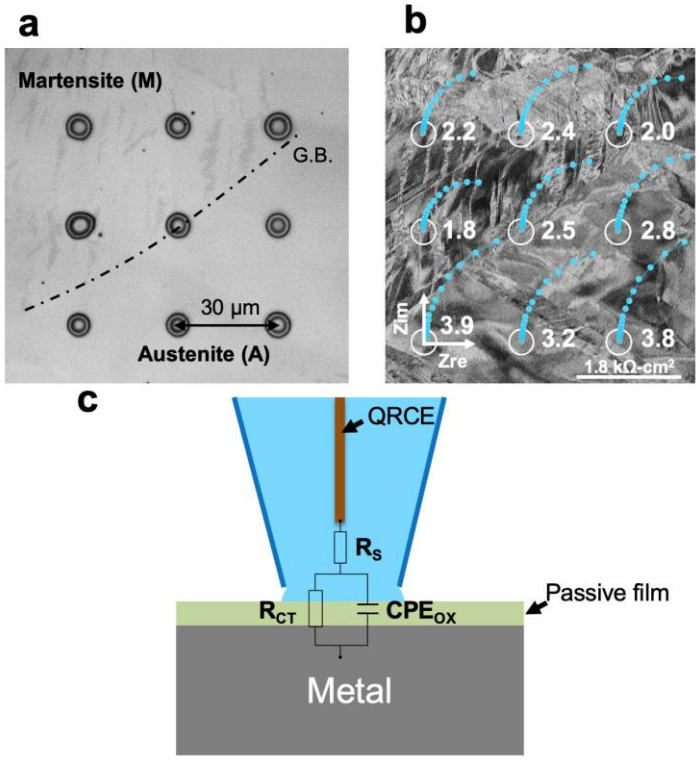

Figure 11. Intragranular scanning probe impedance analysis performed by using a micropipette filled with a 20 mM LiCl + 5 % HNO_3 solution: (a) Optical image showing the matrix of microdroplets covering a martensite-austenite grain boundary (G.B.) in a 30% deformed 304L. (b) Nyquist plots of the localized impedance spectra (real impedance, Zre against imaginary impedance, Zim) in superposition with the backscattered electron image. The spectra were fitted using the Randle circuit (shown in c) and plotted as solid lines in comparison with experimental data (plotted as dots). (c) Illustration of the Randle circuit in correlation to the droplet-passive film-metal configuration.

3.5 Determining SCC susceptibility at micro- to macro- scales.

The scanning EIS spectra yields accurate characteristics of the structural, resistant, and capacitive information of the passivation layer. However, extracting a full spectrum at each location can be time-consuming and therefore limited the efficiency of high-resolution scans. In order to accommodate fast-scanning of larger matrices, constant-frequency scan was developed wherein the magnitude of impedance (|Z|) was captured at a fixed frequency. Because the differences in |Z| were manifested at lower frequencies (see **Figure 11b**), |Z| was mapped at 1 Hz at micro- to macro- scales.

At first, we applied the constant frequency mapping at a localized scale (100 μm×100 μm), wherein non-uniform strain distribution was also induced by the δ-ferrite. As shown in the PLM image (**Figure 12b**), strain-induced deformation bands and α'-martensite are evident surrounding elongated islands of δ-ferrite. Just by using a 11×11 matrix of microdroplets, the strain localization areas were outlined by the AC-impedance map (**Figure 12c**). Consistently, much lower $|Z|_{1Hz}$ were possessed by near-ferrite regions (1.8 ± 0.1 kΩ-cm^2, upper portion of **Figures 12b-c**) as compared to less deformed areas (>2.1 kΩ-cm^2, lower portion of **Figures 12b-c**). The acquired $|Z|_{1Hz}$ are compatible with the R_{CT} values determined in full-spectrum EIS tests. As a result, the constant-frequency impedance map discloses allocations of strain-induced microstructures and their corrosion resistance, and therefore, leading to SCC susceptibility profiling at microscales.

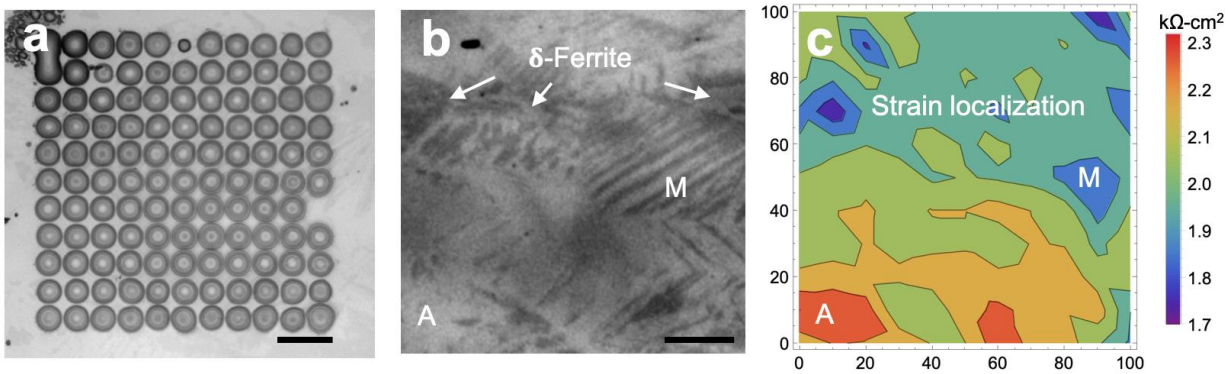

Figure 12. Scanning probe impedance analysis: constant frequency mapping at the microscale. (a) Polarized light microscope (PLM) image show the 11 × 11 microdroplet matrix on a 30% deformed 304L with sampling points located 10 μm apart. A 20 mM LiCl + 5 % HNO_3 solution was used in this scan. (b) PLM image revealing stain localization in the same area after droplets were removed. Note that the surface showed no sign of corrosion even with the aggressive solution used herein. (c) contour plots of the AC-impedance at 1 Hz ($|Z|_{1Hz}$) show promising correlation between corrosion resistance and strain localization. The scale bars are 20 μm in length.

Even though microscale analysis elucidates SCC-susceptible microstructures, it should be compensated by bulk analysis revealing stress and strain concentrated regions. For instance, SCC cracks preferably initiate from localized plastic zone – whether pre-induced[6,45] or developed in-service[46] – distributed across bulk scales[47]. We have accordingly applied the scanning AC-impedance analyses, both full-spectrum and constant frequency, to examine a deformed-to-fracture 304L tensile specimen. The characterized sample provides ideal bulk strain distribution. As shown by the optical image and finite element simulation (**Figures 13a-b**), plastic strain progressively increased from the head to gauge and peaked at the fracture end. Full-spectrum EIS was performed at six locations along the path of neck-gauge-head, and EIS spectra evolved progressively with respect to examined locations (see **Figure 13c**). The corrosion resistance (R_{CT}) was then regressed. Interestingly, the distribution of R_{CT} values is reversely congruent with that of simulated plastic strain (see **Figure 13d**), indicating the distribution of plastic zones can be revealed electrochemically.

Constant-frequency impedance ($|Z|_{1Hz}$) map can disclose more detailed strain localization at the necking area. A scan was conducted over a 0.7 mm × 0.7 mm area at the neck region. Despite difficulty determining the strain distribution over such a large area by conventional means, it is illustrated using the finite element simulation (**Figure 13f**). As denoted by the white arrows in **Figure 13f**, at the severely deformed region near the fractured region, the large plastic strain was more concentrated at the center part. This is in line with the arc-shaped fractural rim shown in the optical image (**Figure 13e**). However, beyond the fracture surface towards the head, the center part experienced less deformation as compared to the edges (see the black arrows in **Figure 13f**). Such strain distribution is depicted in the map of $|Z|_{1Hz}$, which outlines the center region with greater magnitude of AC-impedance as compared to less-resistant edges. The combined results demonstrated that, the scanning AC-impedance analyses can accurately profile plastic strain and the corresponding corrosion resistance, at the same time, at flexible scales. It therefore provides valuable pathways in tracing root-causes of deformed, cracked, and failed nuclear components.

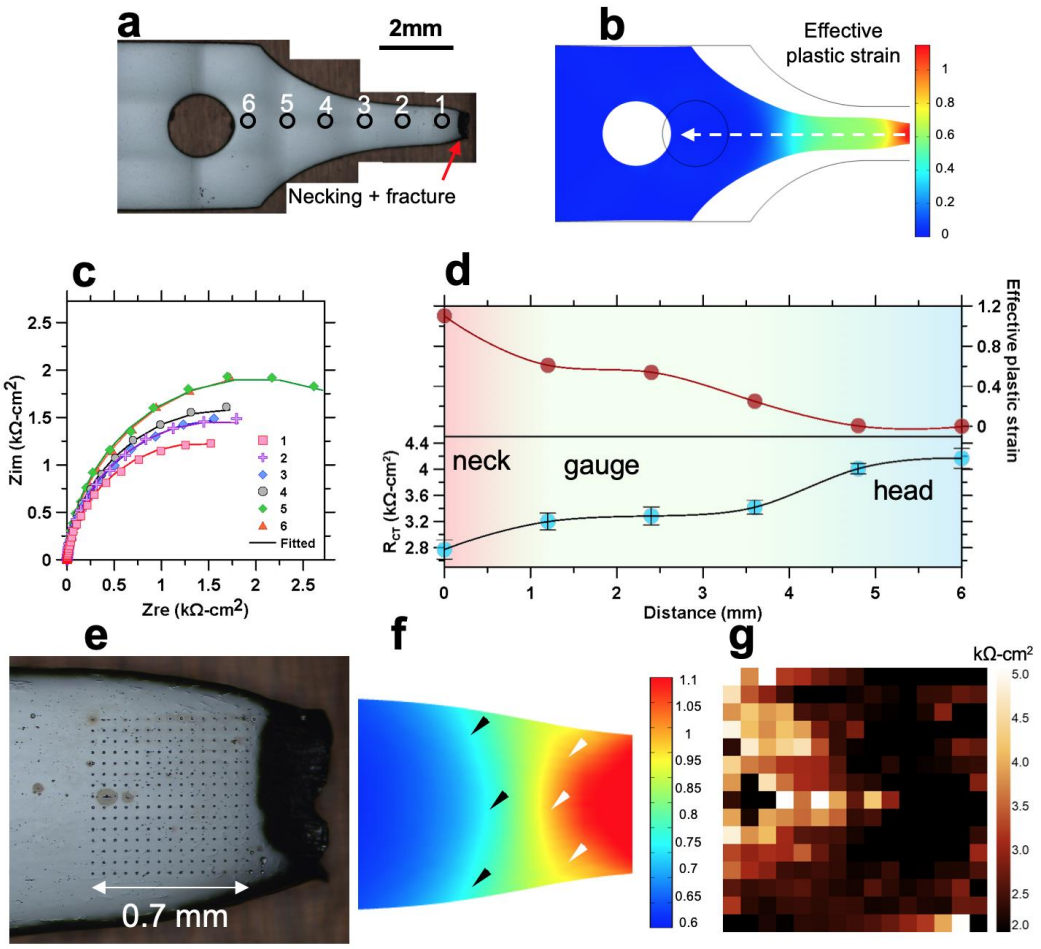

Figure 13. Scanning probe impedance analyses: full-spectrum and constant frequency impedance mapping at the bulk scales. (a) Light microscopy image shows the deformed-to-fracture 304L and locations where the AC-impedance analyses were performed. (b) COMSOL simulation of the stain distribution at the bulk scale. The shape of the unstressed specimen is outlined by the solid black lines. (c) AC-impedance spectra acquired at the locations shown in (a). And the regressed R_{CT} values are plotted in (d), along with simulated effective strain at the same locations. (e) Constant frequency mapping focusing on the necking region, the strain distribution at the same location was simulated and shown in (f). (g) Matrix plot of AC-impedance at 1Hz ($|Z|_{1Hz}$) that is in agreement with the simulated strain distribution.

3.6 Assessing the impact of irradiation-induced damages

Irradiation-induced damages have always been difficult to quantify experimentally and nondestructively. Its impact on corrosion properties is also not fully understood. As irradiation hardens the steel due to defects encompassing point defects, dislocation loops, etc., which are similar, in a sense, to the strain-induced lattice defects. Herein, we exploit the use of AC-impedance to assess the irradiation-induced damages, as a whole, affecting the surface electrochemical reactivities. As shown in **Figure 14a**, a solution annealed 304L steel was partially irradiated at 300 °C by 2 MeV proton ion ($[H^+]$) until a damage dose of 1.11 dpa was attained. The targeted irradiated area is

about 1.5 mm in length but irradiation left no marks on the surface. Nevertheless, the irradiated area was clearly outlined by the impedance ($|Z|_{1Hz}$) map (**Figure 14b**), wherein much lower surface impedances were attained, implying greater surface reactivity. The evolution of $|Z|_{1Hz}$ correlates well with the hardness profile across irradiated and unirradiated areas (**Figure 14c**). Statistical analysis shows that, the 1.1 dpa region were hardened to 209 ± 10 HV as compared to the 148 ± 11 HV for the 0 dpa region, meanwhile $|Z|_{1Hz}$ increased from 2.1 ± 0.5 kΩ-cm^2 to 3.7 ± 0.6 kΩ-cm^2. Interestingly, progressive (somewhat linear) crossover in hardness and $|Z|_{1Hz}$ values were observed at the boundary instead of abrupt transitions, implying the AC-impedance mapping is sensitive to, and therefore can be applied to quantify even smaller irradiation doses. Apparently, scanning AC-impedance mapping disclose detrimental impacts on surface passivation and reactivities provisioned by not only mechanical deformation, but also irradiation-induced damages. The advantages render the scanning probe technique appropriate to profile not only for SCC, but also IASCC susceptibilities, at flexible scales.

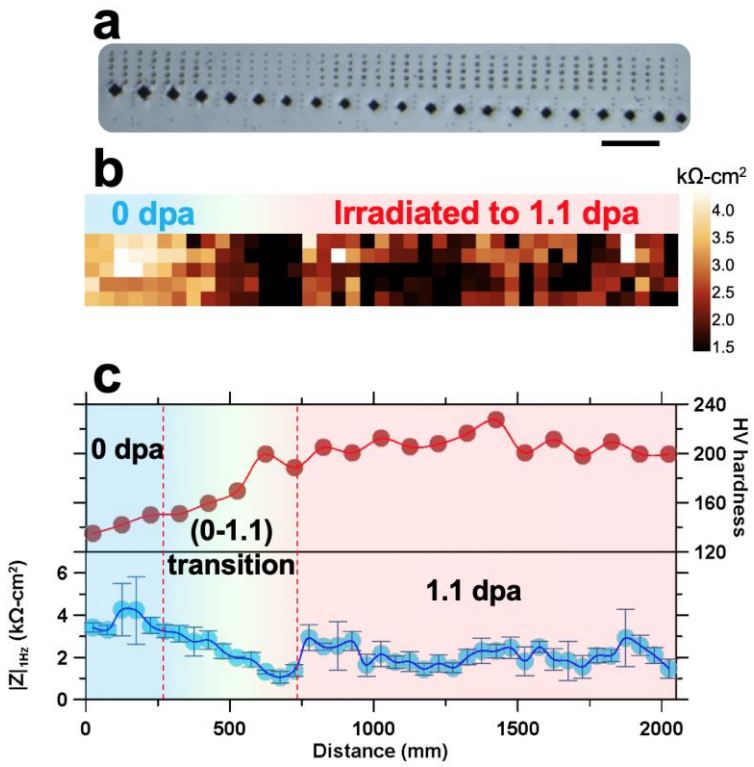

Figure 14. Scanning probe impedance analysis: constant frequency mapping of irradiated 304L. (a) An optical image showing matrices of microdroplets and hardness indents. The microdroplets are 50 μm apart and the hardness indents are 100 μm apart. The scale bar is 200 μm in length. (b) Matrix plot of AC-impedance at 1Hz reveals the boundary of irradiated and unirradiated regions. The averaged $|Z|_{1Hz}$ values at each location are plotted along with the hardness values and shown in (c).

4. Conclusions

Taken together, this work developed multiscale and multimodal approaches to electrochemically profile physical and corrosion damages in nuclear alloys. We determined that, deformation and irradiation induced microstructures elevated the steel's corrosion reactivity, which can be quantified by using scanning probe techniques. Indeed, we have obtained consistent corrosion rate and surface impedance in agreement with allocations and magnitudes of strain concentrations and dpa doses. Specifically, localization of post-yielding microstructures induces the micro-galvanic corrosion in stainless steels. Both deformation- and irradiation- induced damages proportionally demote corrosion impedance and can be mapped at micro-to-macro scales. The methodology developed herein can be utilized to determine and predict SCC and IASCC susceptibilities while accommodating the complex geometry of nuclear alloy components. More importantly, as next generation reactors (e.g. the transformational Challenge Reactor, TCR) will likely employ additive manufacturing (i.e., selective laser melting, SLM) to adapt an agile and continuously evolving design, the outcome of this work can also provide accurate and high-throughput approaches, screening the microstructural heterogeneities and degradation performances of the printed components.

5. References

(1) Cattant, F.; Crusset, D.; Féron, D. Corrosion Issues in Nuclear Industry Today. *Materials today* **2008**, *11* (10), 32–37.

(2) Gussev, M. N.; Leonard, K. J. In Situ SEM-EBSD Analysis of Plastic Deformation Mechanisms in Neutron-Irradiated Austenitic Steel. *Journal of Nuclear Materials* **2019**, *517*, 45–56.

(3) Gussev, M. N.; Field, K. G.; Busby, J. T. Strain-Induced Phase Transformation at the Surface of an AISI-304 Stainless Steel Irradiated to 4.4 Dpa and Deformed to 0.8% Strain. *Journal of Nuclear Materials* **2014**, *446* (1–3), 187–192.

(4) Chen, X.; Gussev, M.; Balonis, M.; Bauchy, M.; Sant, G. Emergence of Micro-Galvanic Corrosion in Plastically Deformed Austenitic Stainless Steels. *Materials & Design* **2021**, 109614.

(5) Matsubara, N.; Kobayashi, T.; Fujimoto, K.; Nomura, Y.; Chigusa, N.; Hirano, S. Research Programs on SCC of Cold-Worked Stainless Steel in Japanese PWR NPP. In *International Symposium Fontevraud*; 2011; Vol. 7, p A099.

(6) Takakura, K.; Nakata, K.; Ando, M.; Fujimoto, K.; Wachi, E. Lifetime Evaluation for IASCC Initiation of Cold Worked 316 Stainless Steel's BFB in PWR Primary Water. In *Proceedings of the 13th International Conference on Environmental Degradation of Materials in Nuclear Power Systems*; 2007.

(7) Was, G. S.; Andresen, P. L. Irradiation-Assisted Stress-Corrosion Cracking in Austenitic Alloys. *JOM* **1992**, *44* (4), 8–13.

(8) Shen, Y. F.; Li, X. X.; Sun, X.; Wang, Y. D.; Zuo, L. Twinning and Martensite in a 304 Austenitic Stainless Steel. *Materials Science and Engineering: A* **2012**, *552*, 514–522.

(9) Liu, T.; Reese, E. R.; Ghamarian, I.; Marquis, E. A. Atom Probe Tomography Characterization of Ion and Neutron Irradiated Alloy 800H. *Journal of Nuclear Materials* **2021**, *543*, 152598.

(10) Calcagnotto, M.; Ponge, D.; Demir, E.; Raabe, D. Orientation Gradients and Geometrically Necessary Dislocations in Ultrafine Grained Dual-Phase Steels Studied by 2D and 3D EBSD. *Materials Science and Engineering: A* **2010**, *527* (10–11), 2738–2746.
(11) Dwivedi, S. K.; Vishwakarma, M.; Soni, A. Advances and Researches on Non Destructive Testing: A Review. *Materials Today: Proceedings* **2018**, *5* (2), 3690–3698.
(12) Chen, Z.; Yusa, N.; Miya, K. Enhancements of Eddy Current Testing Techniques for Quantitative Nondestructive Testing of Key Structural Components of Nuclear Power Plants. *Nuclear engineering and design* **2008**, *238* (7), 1651–1656.
(13) Jiao, Z.; Was, G. Oxidation of a Proton-Irradiated 316 Stainless Steel in Simulated BWR NWC Environment. In *Proceedings of the 15th International Conference on Environmental Degradation of Materials in Nuclear Power Systems—Water Reactors*; Springer, 2011; pp 1329–1338.
(14) Lozano-Perez, S.; Kruska, K.; Iyengar, I.; Terachi, T.; Yamada, T. The Role of Cold Work and Applied Stress on Surface Oxidation of 304 Stainless Steel. *Corrosion Science* **2012**, *56*, 78–85.
(15) McCafferty, E. Introduction to Corrosion Science. 2010. *Alexandria: Springer*.
(16) Andresen, P. L. Stress Corrosion Cracking of Current Structural Materials in Commercial Nuclear Power Plants. *Corrosion* **2013**, *69* (10), 1024–1038.
(17) Was, G. S. *Fundamentals of Radiation Materials Science: Metals and Alloys*; Springer, 2016.
(18) Deng, P.; Peng, Q.; Han, E.-H.; Ke, W.; Sun, C.; Jiao, Z. Effect of Irradiation on Corrosion of 304 Nuclear Grade Stainless Steel in Simulated PWR Primary Water. *Corrosion Science* **2017**, *127*, 91–100.
(19) Daviddi, E.; Gonos, K. L.; Colburn, A. W.; Bentley, C. L.; Unwin, P. R. Scanning Electrochemical Cell Microscopy (SECCM) Chronopotentiometry: Development and Applications in Electroanalysis and Electrocatalysis. *Analytical chemistry* **2019**, *91* (14), 9229–9237.
(20) Mariano, R. G.; Kang, M.; Wahab, O. J.; McPherson, I. J.; Rabinowitz, J. A.; Unwin, P. R.; Kanan, M. W. Microstructural Origin of Locally Enhanced CO 2 Electroreduction Activity on Gold. *Nature Materials* **2021**, 1–7.
(21) Kazakova, O.; Panchal, V.; Burnett, T. L. Epitaxial Graphene and Graphene–Based Devices Studied by Electrical Scanning Probe Microscopy. *Crystals* **2013**, *3* (1), 191–233.
(22) Bever, M. B.; Holt, D. L.; Titchener, A. L. The Stored Energy of Cold Work. *Progress in materials science* **1973**, *17*, 5–177.
(23) Olson, G. B.; Cohen, M. Kinetics of Strain-Induced Martensitic Nucleation. *Metallurgical transactions A* **1975**, *6* (4), 791.
(24) Czerwinski, F.; Cho, J. Y.; Brodtka, A.; Zielinska-Lipiec, A.; Sunwoo, J. H.; Szpunar, J. A. The Edge-Cracking of AISI 304 Stainless Steel during Hot-Rolling. *Journal of materials science* **1999**, *34* (19), 4727–4735.
(25) Cios, G.; Tokarski, T.; Żywczak, A.; Dziurka, R.; Stępień, M.; Marciszko, M.; Pawłowski, B.; Wieczerzak, K.; Bała, P. The Investigation of Strain-Induced Martensite Reverse Transformation in AISI 304 Austenitic Stainless Steel. *Metallurgical and Materials Transactions A* **2017**, *48* (10), 4999–5008.

(26) Shin, H. C.; Ha, T. K.; Chang, Y. W. Kinetics of Deformation Induced Martensitic Transformation in a 304 Stainless Steel. *Scripta Materialia* **2001**, *45* (7), 823–829.
(27) Hack, H. P. Evaluating Galvanic Corrosion. *Anonymous ASM Handbook* **2003**, *13*, 562–567.
(28) Glass, R. S.; Overturf, G. E.; Van Konynenburg, R. A.; McCright, R. D. Gamma Radiation Effects on Corrosion—I. Electrochemical Mechanisms for the Aqueous Corrosion Processes of Austenitic Stainless Steels Relevant to Nuclear Waste Disposal in Tuff. *Corrosion Science* **1986**, *26* (8), 577–590.
(29) Chen, X.; Ebert, W. L.; Indacochea, J. E. Electrochemical Corrosion of a Noble Metal-Bearing Alloy-Oxide Composite. *Corrosion Science* **2017**, *124*, 10–24.
(30) Raiman, S. S.; Bartels, D. M.; Was, G. S. Radiolysis Driven Changes to Oxide Stability during Irradiation-Corrosion of 316L Stainless Steel in High Temperature Water. *Journal of Nuclear Materials* **2017**, *493*, 40–52.
(31) Bard, A. J.; Faulkner, L. R. *Electrochemical Methods: Fundamentals and Applications*, 2nd ed.; John Wiley & Sons, 2001; Vol. 2.
(32) Sidane, D.; Devos, O.; Puiggali, M.; Touzet, M.; Tribollet, B.; Vivier, V. Electrochemical Characterization of a Mechanically Stressed Passive Layer. *Electrochemistry Communications* **2011**, *13* (12), 1361–1364.
(33) Sidane, D.; Touzet, M.; Devos, O.; Puiggali, M.; Larivière, J. P.; Guitard, J. Investigation of the Surface Reactivity on a 304L Tensile Notched Specimen Using Scanning Electrochemical Microscopy. *Corrosion Science* **2014**, *87*, 312–320.
(34) Zhu, R. K.; Luo, J. L. Investigation of Stress-Enhanced Surface Reactivity on Alloy 800 Using Scanning Electrochemical Microscopy. *Electrochemistry Communications* **2010**, *12* (12), 1752–1755.
(35) Hurley, M. F.; Efaw, C. M.; Davis, P. H.; Croteau, J. R.; Graugnard, E.; Birbilis, N. Volta Potentials Measured by Scanning Kelvin Probe Force Microscopy as Relevant to Corrosion of Magnesium Alloys. *Corrosion* **2014**, *71* (2), 160–170.
(36) Cheon, J. Y.; Kim, J. H.; Kim, J. H.; Goddeti, K. C.; Park, J. Y.; Joo, S. H. Intrinsic Relationship between Enhanced Oxygen Reduction Reaction Activity and Nanoscale Work Function of Doped Carbons. *Journal of the American Chemical Society* **2014**, *136* (25), 8875–8878.
(37) Schmutz, P.; Frankel, G. S. Characterization of AA2024-T3 by Scanning Kelvin Probe Force Microscopy. *Journal of the Electrochemical Society* **1998**, *145* (7), 2285–2295.
(38) Verchère, L.; Aubert, I.; Devos, O. Influence of the Crystallographic Orientation on the Electrochemical Reactivity Measured by Scanning Electrochemical Microscopy on Nickel-Based Alloy 600. *Electrochimica Acta* **2019**, *313*, 292–302.
(39) Singh, K. K. Strain Hardening Behaviour of 316L Austenitic Stainless Steel. *Materials science and technology* **2004**, *20* (9), 1134–1142.
(40) Shen, Z.; Du, D.; Zhang, L.; Lozano-Perez, S. An Insight into PWR Primary Water SCC Mechanisms by Comparing Surface and Crack Oxidation. *Corrosion Science* **2019**, *148*, 213–227.
(41) Chang, L.; Volpe, L.; Wang, Y. L.; Burke, M. G.; Maurotto, A.; Tice, D.; Lozano-Perez, S.; Scenini, F. Effect of Machining on Stress Corrosion Crack Initiation in

Warm-Forged Type 304L Stainless Steel in High Temperature Water. *Acta Materialia* **2019**, *165*, 203–214.
(42) Xu, Y.; Jing, H.; Xu, L.; Han, Y.; Zhao, L. Effect of δ-Ferrite on Stress Corrosion Cracking of CF8A Austenitic Stainless Steels in a Simulated Pressurised Water Reactor Environment. *Journal of Materials Research and Technology* **2019**, *8* (6), 6420–6426.
(43) Lozano-Perez, S.; Yamada, T.; Terachi, T.; Schröder, M.; English, C. A.; Smith, G. D. W.; Grovenor, C. R. M.; Eyre, B. L. Multi-Scale Characterization of Stress Corrosion Cracking of Cold-Worked Stainless Steels and the Influence of Cr Content. *Acta Materialia* **2009**, *57* (18), 5361–5381.
(44) Deng, P.; Peng, Q.; Han, E.-H.; Ke, W. Effect of the Amount of Cold Work on Corrosion of Type 304 Nuclear Grade Stainless Steel in High-Temperature Water. *Corrosion* **2017**, *73* (10), 1237–1249.
(45) Hamilton, M. L.; Huang, F.-H.; Yang, W. J.; Garner, F. A. Mechanical Properties and Fracture Behavior of 20% Cold-Worked 316 Stainless Steel Irradiated to Very High Neutron Exposures. In *Influence of Radiation on Material Properties: 13th International Symposium (Part II)*; ASTM International, 1987.
(46) Was, G. S. *Fundamentals of Radiation Materials Science: Metals and Alloys*; springer, 2016.
(47) Wenman, M. R.; Trethewey, K. R.; Jarman, S. E.; Chard-Tuckey, P. R. A Finite-Element Computational Model of Chloride-Induced Transgranular Stress-Corrosion Cracking of Austenitic Stainless Steel. *Acta materialia* **2008**, *56* (16), 4125–4136.